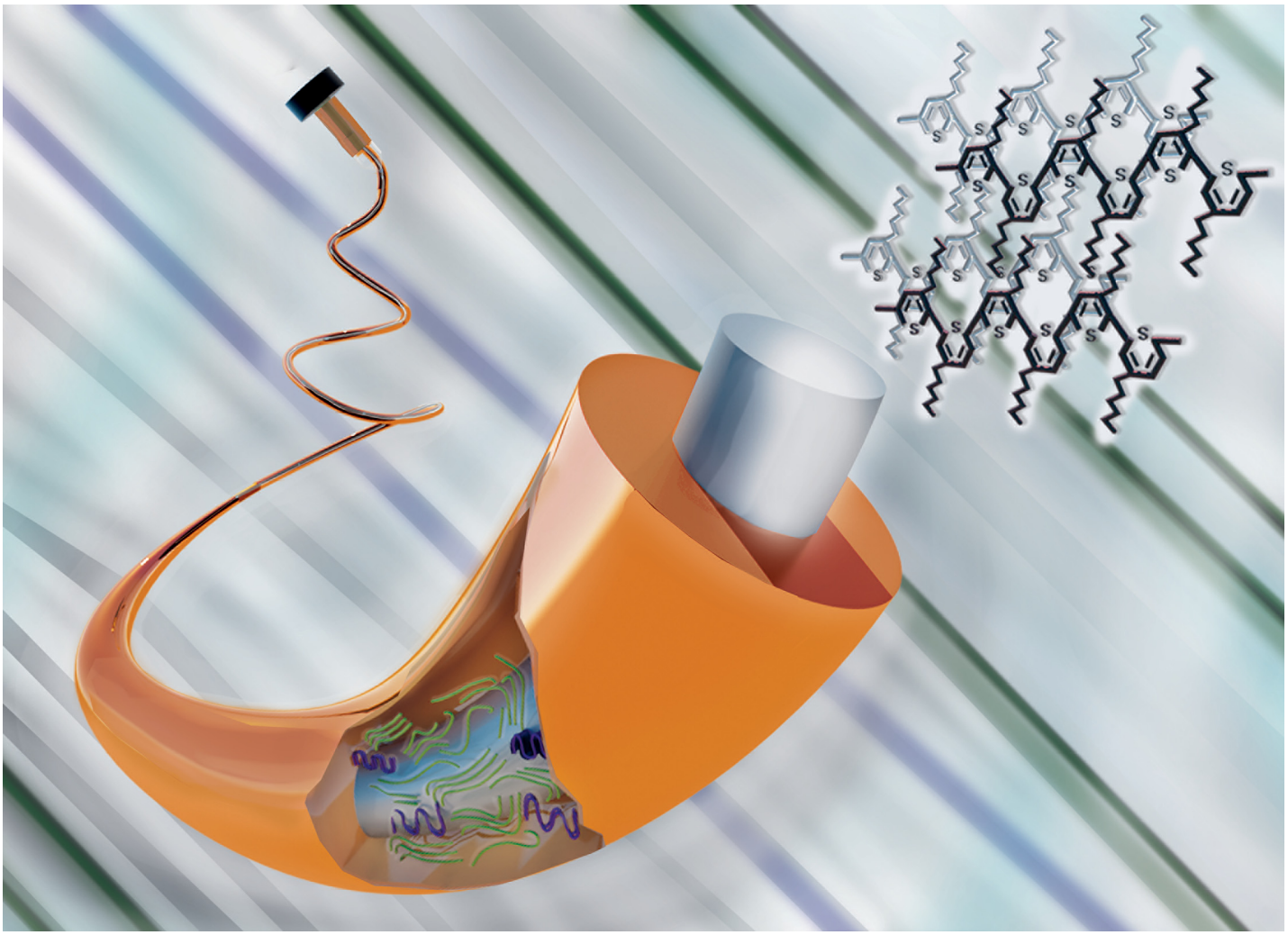

Showcasing research from Professor Santanu Kundu's laboratory, Dave C. Swalm School of Chemical Engineering, Mississippi State University, MS State, United States.

Highly stretchable coaxial P3HT electrospun fibers with enhanced reversibility

Highly stretchable coaxial fibers consisting of semiconducting poly(3-hexylthiophene), and butyl rubber were obtained using a coaxial electrospinning technique. For these highly stretchable fibers, the electrical conductivity of the doped fibers did not change significantly up to 400% strain and showed excellent mechanical reversibility and electrical durability under cyclic loading.

As featured in:

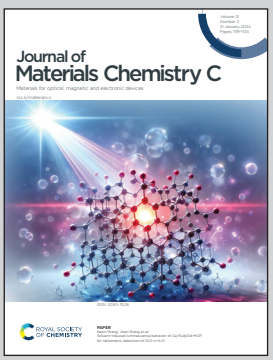

See Santanu Kundu *et al.*, *J. Mater. Chem. C*, 2024, **12**, 884.

ROYAL SOCIETY OF CHEMISTRY

rsc.li/materials-c

Registered charity number: 207890

Journal of Materials Chemistry C

ROYAL SOCIETY OF CHEMISTRY

PAPER

View Article Online
View Journal | View Issue

Cite this: J. Mater. Chem. C, 2024, 12, 884

Highly stretchable coaxial P3HT electrospun fibers with enhanced reversibility†

Humayun Ahmad, [a] Maggie Britton,[a] Mahesh Gangishetty [b] and Santanu Kundu *[a]

Received 23rd August 2023,
Accepted 4th November 2023

DOI: 10.1039/d3tc03027j

rsc.li/materials-c

Conjugated polymers have potential applications in many areas, including stretchable photovoltaic, wearable sensors, electronic skin, and flexible displays. The polymer must maintain electronic properties with mechanical deformation for these applications, particularly repetitive mechanical loading and unloading. Achieving such is a significant challenge, as the performance of many systems deteriorates under stretched conditions. Here, we report the fabrication of highly stretchable coaxial fibers consisting of semiconducting poly(3-hexylthiophene) (P3HT), and butyl rubber (BR) obtained using an electrospinning technique. Because of the presence of P3HT in the shell, these fibers could be easily doped using F4TCNQ. For these highly stretchable fibers, the electrical conductivity for the doped fiber did not change significantly up to 400% strain. Further, the conductivity is maintained for this applied strain under cyclic loading, showing excellent mechanical reversibility and electrical durability of the fibers. Moreover, the presence of P3HT at the shell facilitates the direct doping of the fiber without any post-treatment of the fiber mat. Besides, other polymers were successfully used as a core in the coaxial fibers, demonstrating the general applicability of our spinning approach.

1. Introduction

Conjugated polymers (CPs) are promising candidates for stretchable, wearable, and implantable electronics due to their chemical versatility, solution processability, relatively low cost, and scalability.[1–10] However, CP-based devices often cannot maintain electronic performance when subjected to a repeating or cyclic mechanical loading due to the plastic deformation of CPs, interfacial delamination at the polymer substrate interface, and crack formation and propagation initiated from the internal defects and due to limited extensibility of CPs.[9,11,12] To overcome these problems, several strategies have been reported in the literature, including multi-component systems, such as CPs blended with elastomers, block copolymers with elastomeric blocks, plasticizing CPs with small molecules, and coating elastomers with a CP.[4,11,13–25]

Among all the approaches mentioned above, thin films fabricated from the blends of CPs and elastomers have been thoroughly studied.[16,21–25] Typically, polystyrene–polyethylene–polybutylene–polystyrene (SEBS), polystyrene-*block*-polyisoprene-*block*-polystyrene, and crosslinked polydimethylsiloxane have been used as elastomers.[9,16,19,25–28] The charge carrier mobility of thin films consisting of a blend of polydiketopyrrolopyrrole (PDPP) and SEBS was recorded as high as 1 $cm^2 V^{-1} s^{-1}$ at 100% strain.[28] The fracture strain for this system was 300%, but a decrease in charge carrier mobility was observed beyond 100% applied strain. Bao and coworkers developed a terpolymer-based semiconductor comprising three discrete conjugated building blocks with high mobility and mechanical reversibility.[9] This terpolymer thin film could sustain >100% strain without crack formation and displayed high mechanical reversibility. Typically, the blending of insulating elastomers in CPs hampers the charge-carrier mobility of CPs.[29] Thus, for stretchable systems, it is desirable to devise a simple approach that avoids blending multiple components to preserve the electrical properties of CPs, particularly at the stretched condition and subjected to cyclic mechanical loading.

In many functional applications, CPs processed into fiber form is beneficial. The fibers can be obtained using the electrospinning (ES) method, in which coaxial geometry can be implemented with CPs in the core or shell without any additives, avoiding the limitations of the blended systems.[29–32]

[a] Dave C. Swalm School of Chemical Engineering, Mississippi State University, MS State, MS 39762, USA. E-mail: santanukundu@che.msstate.edu
[b] Department of Chemistry & Department of Physics and Astronomy, Mississippi State University, MS 39762, USA

† Electronic supplementary information (ESI) available: Experimental set-up for stretching experiments showing fiber mat collected on a paper cut; optical microscope (OM) image of two fibers crossings on Au coated electrode; OM image of beaded fibers from P3HT_PMMA; OM of P3HT_BR fibers for different BR concentrations; effects of shell-side solution flow rates; SEM of typical P3HT_BR fibers showing cylindrical shape; TEM cross-section image of P3HT_BR fibers; conductivity determination for a core–shell fiber; *I–V* response of fibers with different core polymers; mechanical stretching of fibers; video of mechanical stretching of fiber mat. See DOI: https://doi.org/10.1039/d3tc03027j

Further, rapid evaporation of the solvent in electrospun micro/nanofiber results in kinetically frozen polymer chains, which reduces overall crystallinity and longer-range ordered aggregates.[33,34] These fibers are promising candidates for stretchable optoelectronic devices because a significant fraction of disordered amorphous domains provides the desired stretchability and reversibility during their applications.[11]

In the past, a two-fluid coaxial ES technique was utilized by maintaining poly(3-hexylthiophene) (P3HT) as the core and poly(methyl methacrylate) (PMMA) as the shell.[32,34] Here, the PMMA shell was selectively removed using acetone, a process known as solvent etching. Coaxial fibers with P3HT as a core and semicrystalline polyethylene oxide (PEO) as a shell have also been reported.[29] The PEO shell was removed, and these fibers were then investigated in the FET devices. A high hole mobility of 8.58×10^{-2} cm^2 V^{-1} s^{-1} under 100% strain has been reported.[29] Similarly, polyurethane (PU) was utilized as a stretchable core, whereas poly(3,3‴-didodecylquaterthiophene) (PQT-12) was used as a shell.[17] Both, PU and PQT-12 were mixed with PEO at ratios of 1 : 1 and 2 : 1 w/w, respectively, to achieve sufficient viscosity for facilitating electrospinning. These coaxial electrospun fiber-based transistors maintained good operational stability under mechanical strains up to 30%.

The above examples lack a complete understanding of the structure formation of CPs during processing and the evolution of those structures during mechanical loading, particularly the underlying mechanism responsible for mechanical reversibility. In fact, an understanding of the processing-structure–property relationship at large strain for CP fiber-based systems remains scarce. This is contrary to the thin-film based systems, where a significant understanding regarding the charge transport properties subjected to mechanical loading has been achieved.

This study reports the fabrication of highly stretchable coaxial electrospun fibers. Here, P3HT was in the shell, allowing easy characterization and the subsequent doping process for improved performances. This is contrary to the literature reports where P3HT was mostly in the core, which needed shell removal for characterization and applications.[29,32,34] A low glass transition temperature elastomer, butyl rubber (BR), was used as a core due to its high stretchability. The coaxial fiber composed of P3HT and BR displayed failure strain as high as ≈1000%. Most importantly, these coaxial fibers manifested excellent electrical properties and reversibility under cyclic loading. A sequential doping method for P3HT was employed to improve electrical conductivity. The doped and undoped fiber results were compared with the less stretchable systems including flexible polymers, PEO, and PMMA.

2. Experimental

2.1. Materials and methods

P3HT with M_w ≈ 75 kDa, RR ≈ 95% was purchased from Rieke Metals Inc. (Lincoln, NE). PEO (M_w ≈ 600–1000 kDa), PMMA (M_w ≈ 1000 kDa), chloroform (>99.5%), and acetonitrile were purchased from Sigma-Aldrich. Butyl rubber (EXXON™ Butyl 068) was donated by ExxonMobil Corporation. The dopant F4TCNQ was purchased from Ossila Inc. All chemicals and polymers were used as received.

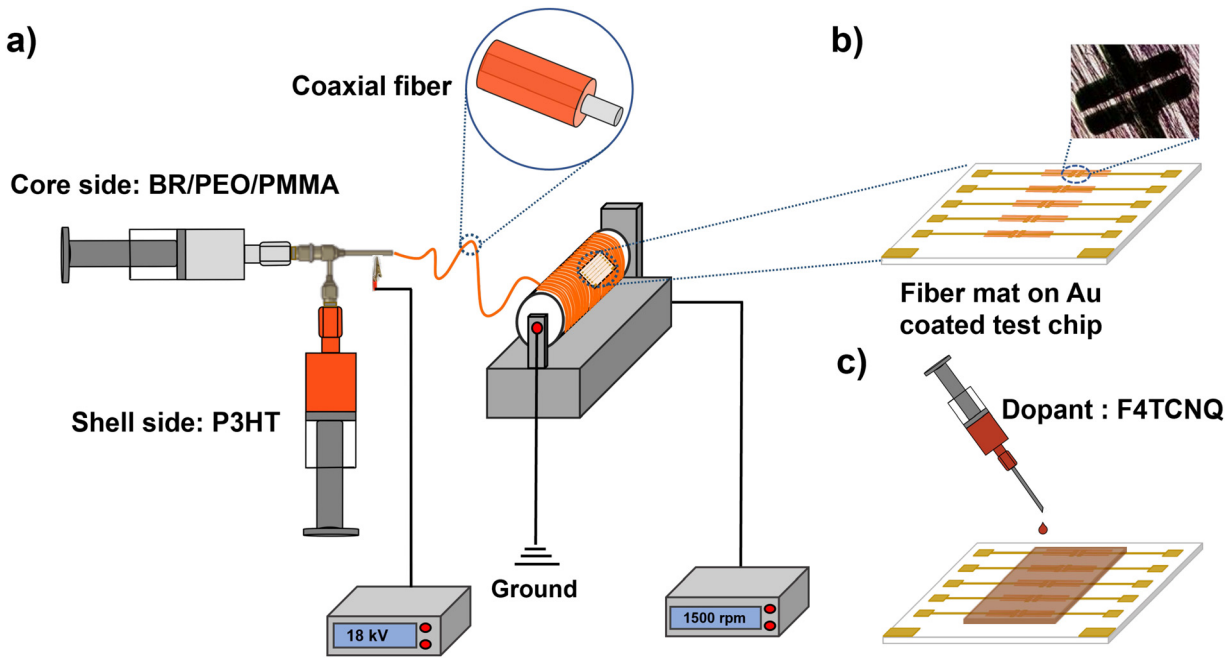

Fig. 1 (a) Schematic of a coaxial-electrospinning setup for spinning core–shell fibers. (b) Fiber mat collected on gold coated test chip, inset showing the optical microscope image of the fiber mat; (c) sequential fiber doping process.

2.2. Sample preparation

Separate solutions of P3HT, PEO, PMMA, and BR in chloroform with concentrations of 3, 1, 20, and 10% (wt/v), respectively, were prepared in individual glass vials. The P3HT, PEO, PMMA, and BR solutions were stirred on a magnetic hot plate at 55 °C for two, two, six hours, and overnight, respectively. These vials were tightly sealed to avoid chloroform evaporation.

2.3 Electrospinning process

Fig. 1 depicts a schematic of the ES setup considered here. It utilizes two syringes containing core and shell precursor solutions and a coaxial flat-tip needle with 22 and 18 inner and outer gauges, respectively. P3HT was used as a shell solution, whereas PEO/PMMA/BR was used as the core solution. These coaxial fibers are denoted herein as P3HT_PEO, P3HT_PMMA. P3HT_BR, respectively. The flow rate of the core and shell solutions was maintained at 1.0 and 0.5 mL h^{-1}, respectively, by using two syringe pumps (NE-1000, NewEra Pump Systems Inc.). The needle tip was connected to a high-voltage power supply (RC-5000, Tong Li Tech, China). An 18 kV power, 1500 rpm, and 8 cm tip-to-needle distance were maintained for all experiments. The experiments were conducted at room temperature (20 °C) with relative humidity ranging from 35 to 45%.

2.4. Stretching experiments

A custom-built setup was used to perform stretching experiments on fiber mats. Fiber mats were collected by placing paper frames on the rotational collector (Fig. S1a, ESI†). The paper frames were supported on the experimental setup using two rectangular aluminum frames (Fig. S1b, ESI†). The samples were stretched uniaxially using a moving stage (PI M414.3PD, Physik Instrumente, Germany). A constant strain rate of 4%/s was considered here. The fiber collection and stretching tests were conducted on the same day to minimize environmental effects. At least three samples were tested from the same batch, and the average values are reported here.

2.5. Sequential doping

This study used the strong electron acceptor 2,3,5,6-tetrafluoro-7,7,8,8-tetra-cyanoquinodimethane (F4TCNQ) as a dopant. The coaxial P3HT fibers were collected on a quartz-coated glass substrate with an array of gold contacts. The collected fibers were doped by adding F4TCNQ solution in acetonitrile (0.1 mg mL^{-1}) dropwise. The samples were subsequently dried for further characterization.

2.6. Characterization

The FE-SEM study was carried out using JEOL JSM-6330F instrument at an accelerating voltage of 5 kV to image the electrospun fiber mat on aluminum foil. The electrospun fiber mat was sputter-coated with an approximately 15 nm thick platinum layer to avoid charging. The fiber diameters were estimated using image processing software (ImageJ). TEM images were captured at 200 kV using JEOL JEM 2100 with LaB6 emitter fitted with Oxford Instrument's X-maX 80 T detector. The fiber mat was collected on double-sided tape. The fiber mat was embedded in LR White acrylic resin and cured overnight at room temperature. Once the specimen block had hardened, it was sectioned using Reichert Jung Ultracut E Microtome. The 60–70 nm microtome sections were analyzed using JEOL 2100 (Lab6) TEM at 200 kV. Uranyl acetate was used as a staining agent for TEM measurements.

The photoluminescence (PL) study of fiber mats was performed using an Edinburgh FS5 Spectrofluorometer instrument. The fiber mats were collected on the 15 mm × 20 mm quartz-coated glass substrates. The excitation wavelength of 450 nm was used. The emission scans were collected over the 500 to 800 nm range using a slit width of 4–5 nm with a 1 nm wavelength increment and an integration time of 1 s. The instrument displays a maximum peak position variation of as high as ±3 nm.

POM images were obtained using a MEIJI Techno MT9000 optical microscope equipped with a polarizer, rotatable analyzer, rotatable stage, first-order retardation plate, and a 7MP Sony Pregius Gen3 camera. The electrical conductivity of electrospun fibers (doped and undoped) was measured using a custom-built multipin framework, and the details regarding the setup can be found in our prior work.[35] Briefly, electrospun fibers were collected on a quartz-coated glass substrate with an array of gold contacts (Fig. S2, ESI†). The distance between two neighboring gold contacts ranges from 30 to 80 μm. An optical microscope image was used to identify the number of fibers connecting two neighboring gold contacts and the fiber diameters. A Keithley source meter (2604B, dual-channel, 40V SMU) was used to measure the *I*–*V* response over the applied voltage range of −2 to +2 V. For single fiber and fiber mat conductivity measurements, at least six independent data points from different batches were collected and presented using a boxplot to show the data distribution through their quartiles.

2.7. Statistical analysis

All fiber diameter data are reported as mean ± standard deviation with $n \geq 20$. The average core and shell thickness are also reported as mean ± standard deviation with $n \geq 10$. The conductivity values between the two experimental groups were compared using two-tailed *t*-tests ($\alpha = 0.05$, significance determined at $p < 0.05$).

3. Results and discussion

3.1. Fabrication and morphology of coaxial electrospun fibers

We successfully electrospun coaxial fibers with P3HT in the shell, and flexible polymers, either PEO, PMMA, or BR, in the core. The experimental setup and fiber collection process are shown in Fig. 1a–c. The spinning was performed using freshly prepared solutions (w/o aging) to avoid aging-induced aggregation of P3HT in the solution.[35] The polymers were mixed in chloroform at 55 °C, and after transferring the solutions to the

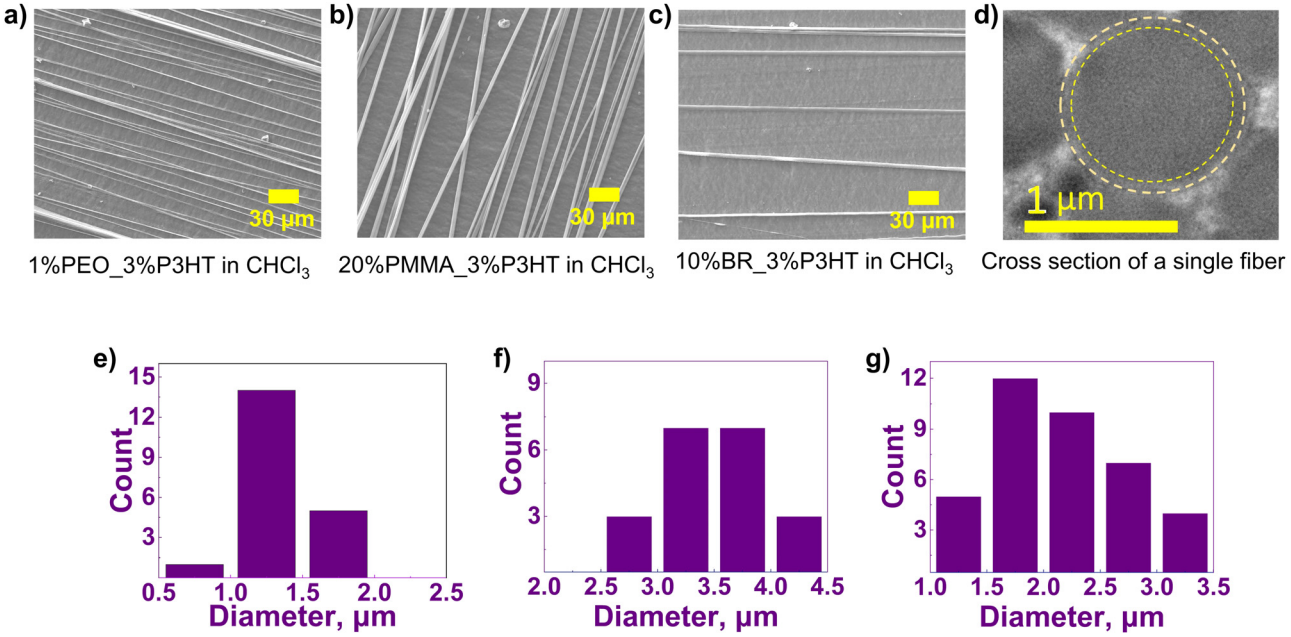

Fig. 2 SEM micrographs of core–shell fibers collected on aluminium foil. SEM images of fibers and their size distribution of: (a) and (e) P3HT_PEO, (b) and (f) P3HT_PMMA, and (c) and (g) P3HT_BR. Here, P3HT is in the shell. (d) TEM image of the cross-section of a P3HT_BR fiber. The dotted annular area highlights the P3HT shell.

syringes, they were allowed to cool to room temperature before spinning. P3HT concentration in the solution was kept constant at 3% (wt/v) for all the experiments. Further, 1% (wt/v) PEO concentration was considered because of its ability to produce fiber, as shown in our previous study.[35] A PMMA concentration of 20% (wt/v) was selected, as beaded fibers were obtained for lower concentrations, *e.g.*, 10% (wt/v) (Fig. S3, ESI†). Similarly, for BR, 3 and 6% (wt/v) concentrations led to beaded fiber, but 10% (wt/v) resulted in bead-less fibers (Fig. S4, ESI†). The core flow rate was maintained constant at 1 mL h^{-1} for these concentrations, and the shell flow rate was optimized. A higher shell flow rate (1 mL h^{-1}) led to beaded fiber formation, whereas the lower shell flow rate (0.1 mL h^{-1}) resulted in fragmented fibers (Fig. S5, ESI†). Thus, the shell flow rate was kept constant at 0.5 mg mL^{-1} for all cases.

The morphology of the P3HT fiber mat was assessed by FE-SEM (Fig. 2). In general, the fibers were cylindrical (Fig. S6, ESI†). The SEM images were used to determine the fiber diameters, and the corresponding histograms for at least 20 single fibers for each case are presented in Fig. 2e–g. The average fiber diameters of coaxial P3HT fibers (Fig. 2a–c) were 1.36 ± 0.21, 3.42 ± 0.57, and 2.20 ± 0.61 μm for PEO, PMMA, and BR, respectively. The flexible polymer concentration in the spinning solution was the highest for PMMA and the lowest for PEO. That led to the largest and smallest fiber diameters for P3HT_PMMA and P3HT_PEO, respectively. Higher polymer concentration leads to higher solution viscosity and lower charge density per chain for the applied voltage. As a result, the polymer chains experience lower stretching force, leading to larger fiber diameters.[36] Fig. 2d displays the TEM image of the cross-section of a P3HT_BR single fiber, and that for multiple fibers can be found in Fig. S7 (ESI†). The core and shell structure is evident in the TEM image. The average shell thickness has been measured as 0.1 ± 0.01 μm, much thinner than the core diameter of 1.1 ± 0.15 μm.

To probe the ordering of P3HT during the ES process, the fiber mat was investigated using cross-polarized light and a first-order retardation plate. The micrograph for a single fiber is shown in Fig. 3. The fiber parallel to the polarizer was completely extinct, but rotating the sample by ±45° with respect to the analyzer led to bright fiber. This birefringence of the fibers indicates the crystalline phase present in the fiber. However, as the color was not either entirely blue or yellow upon rotation indicates that P3HT chains were not uniaxially oriented. Instead, crystalline domains were present in the fiber.

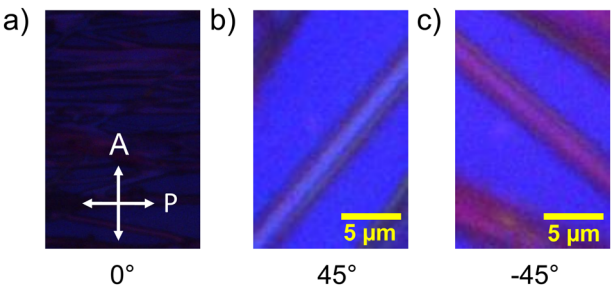

Fig. 3 Polarized optical micrographs of P3HT_BR coaxial fiber under crossed polarized light. (a) Fiber parallel to the polarizer with no waveplate added; (b) and (c) fiber with first retardation plate and rotated 45° to −45° with respect to the analyzer, respectively.

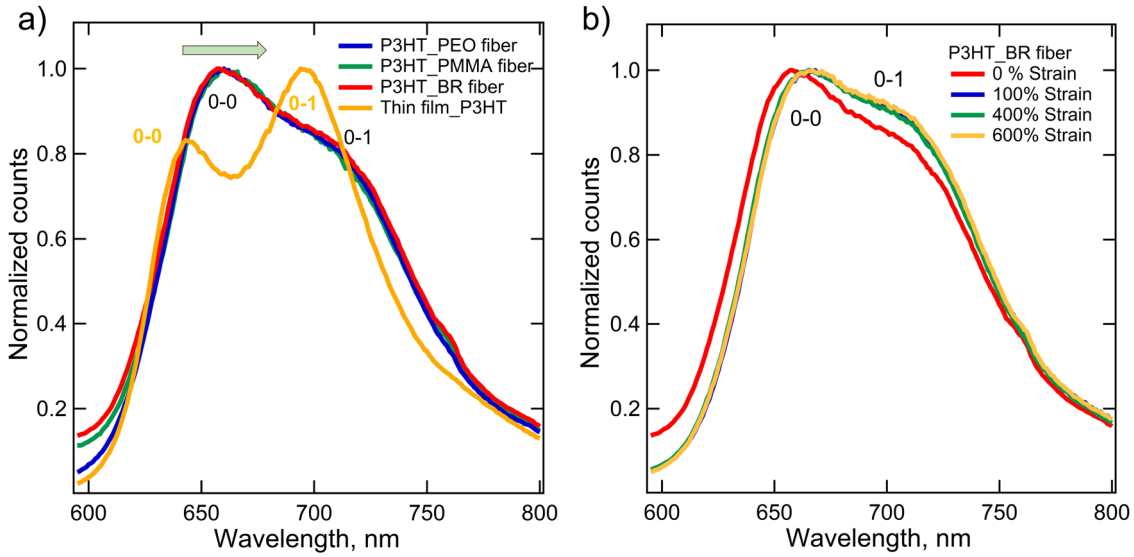

Fig. 4 Normalized PL spectra for (a) pristine P3HT thin film, and fibers (in fiber mat form) with different core polymers, and (b) P3HT_BR ES fibers after subjected to mechanical strain. The excitation wavelength was 450 nm.

3.2. Photophysical properties

Photoluminescence (PL) spectra were collected on the as-spun and mechanically stretched fibers to understand P3HT structure formation, particularly the aggregation of P3HT chains and the change of those structures as a function of mechanical stretching. A custom-built tensile instrument (Fig. S1b, ESI†) was used to stretch the fiber mat to above 1000% of the initial length. The stretched fiber mat was collected immediately on a quartz-coated glass slide to capture the PL data. The fibers adhered to the glass slide because of their stickiness, and care was taken to avoid the sample relaxation.

Fig. 4a displays the PL spectra of as-spun fiber mats (0% strain) with three different core polymers. Data for pristine P3HT thin film (without flexible polymer) is also shown for comparison purposes. Two distinct peaks at ≈645 nm and ≈695 nm were observed for the thin film. For the fiber mat, a sharp peak at ≈660 nm, one broad peak at ≈714 nm, and one shoulder peak around ≈760 nm were observed for all cases. The peaks at ≈645 (thin film) and ≈660 nm (fibers) can be attributed to the 0-0 aggregation of P3HT chains, whereas ≈694 (thin film) and ≈714 nm (fibers) can be attributed to the 0-1 aggregation.[37] The 0-0 and 0-1 transitions correspond to intra-chain and inter-chain excitation coupling, denoting the J- and H-aggregates, respectively.[38] Compared to the thin film, the aggregation peaks for the fibers redshifted by as high as 20 nm. The red-shifted emission indicates more ordered aggregates in the fibers.[32] Specifically, the stretched P3HT chains during electrospinning facilitated the formation of H-aggregates in fibers. No significant differences in peak positions have been observed for three core polymers, indicating that the core did not play a significant role in the structure formation of P3HT on the shell side.

Fig. 4b displays the PL response of the P3HT_BR fibers after mechanical stretching, and the results for 100, 400, and 600% nominal strain values are shown. We chose to investigate P3HT_BR fibers further because of their highest stretchability. The peak at ≈660 nm was slightly redshifted to ≈670 nm with the application of 100% strain, however, no further shift was observed with increasing strain to 600%. In addition, the intensity of the ≈714 nm peak has been found to increase slightly with the application of strain. Note that we have normalized the PL spectra based on the maximum intensity observed for a sample. For the thin film, the maximum intensity was observed for 0-1 peak, whereas, for fibers, it was 0-0. Further, we have seen a slight variation from batch to batch, and the redshift was observed to be as high as 20 nm. The relative increase of the 0-1 peak and redshift of the 0-0 aggregation peak with stretching indicates an increase in the H-aggregate fraction.[39,40] We hypothesize that mechanical stretching leads to the alignment of the amorphous region and subsequent increase in H-aggregation (higher inter-chain interactions).

3.3. Electrical conductivity of the fibers

3.3.1. As-spun fibers. A custom-built system was used to investigate the electrical conductivity (σ) of ES fibers. As detailed earlier, we aim to deposit a single fiber on the electrode. However, collecting a single fiber on a chip consistently was experimentally challenging. We frequently obtained two to four fibers crossing the electrodes (Fig. S2, ESI†).

For a single fiber, the σ of P3HT_BR fibers was estimated by considering the thickness of the P3HT region (annular region) in coaxial fibers using the following equation, $\sigma = \frac{I}{V} \times \frac{L}{A} = \frac{\frac{I}{V}}{\pi\left(\frac{R_1^2 - R_2^2}{L}\right)}$, where A, I, V, L, R_1, and R_2 are the fiber cross-sectional area, current, voltage, length, overall radius, and core radius of the fiber, respectively. The

approximate thickness of the P3HT region was estimated from the cross-sectional image of the fibers (Fig. 2d and Fig. S7, ESI†). The maximum single fiber σ for undoped P3HT_BR was 6.1×10^{-5} S cm^{-1}. Fig. S8 (ESI†) provides further information regarding the σ measurements.

Since obtaining TEM images for every case was challenging, particularly at the stretched condition, we considered the overall radius for single fiber σ measurement. For a single fiber, σ values were obtained by: $\sigma = \frac{I}{V} \times \frac{L}{A} = \frac{\frac{I}{V}}{\pi\left(\frac{R_1^2}{L}\right)}$. For more than one fiber connecting two electrodes, the average σ of those fibers can be estimated as: $\sigma = \frac{\frac{I}{V}}{\pi \sum_{i=1}^{n}\left(\frac{R_i^2}{L_i}\right)}$, where n is the number of the fiber. For the fiber mat, we have considered the area as $A = W \times T$, where W and T are the width of the electrode and thickness of the fiber mat, respectively. The I–V data for each case are shown in Fig. S9 (ESI†). Note that the I–V response depends on the number of fibers connecting the electrodes.

Fig. 5a displays σ for all three core polymers and at the two conditions (undoped and doped). For each case, at least 9 specimens were characterized. For undoped fibers, the maximum single fiber σ for P3HT_BR was estimated as $\approx 9 \times 10^{-6}$ S cm^{-1} by considering the diameter of the fiber as R_1. This value is lower but not significantly different from 6.1×10^{-5} S cm^{-1} estimated considering P3HT in the annular region. For simplicity, we have used this method for the estimation of σ.

The average σ values for undoped P3HT_PEO and P3HT_PMMA were 1.5×10^{-5}, and 5.0×10^{-7} S cm^{-1}, respectively. The σ of P3HT_PEO fibers have been found to be

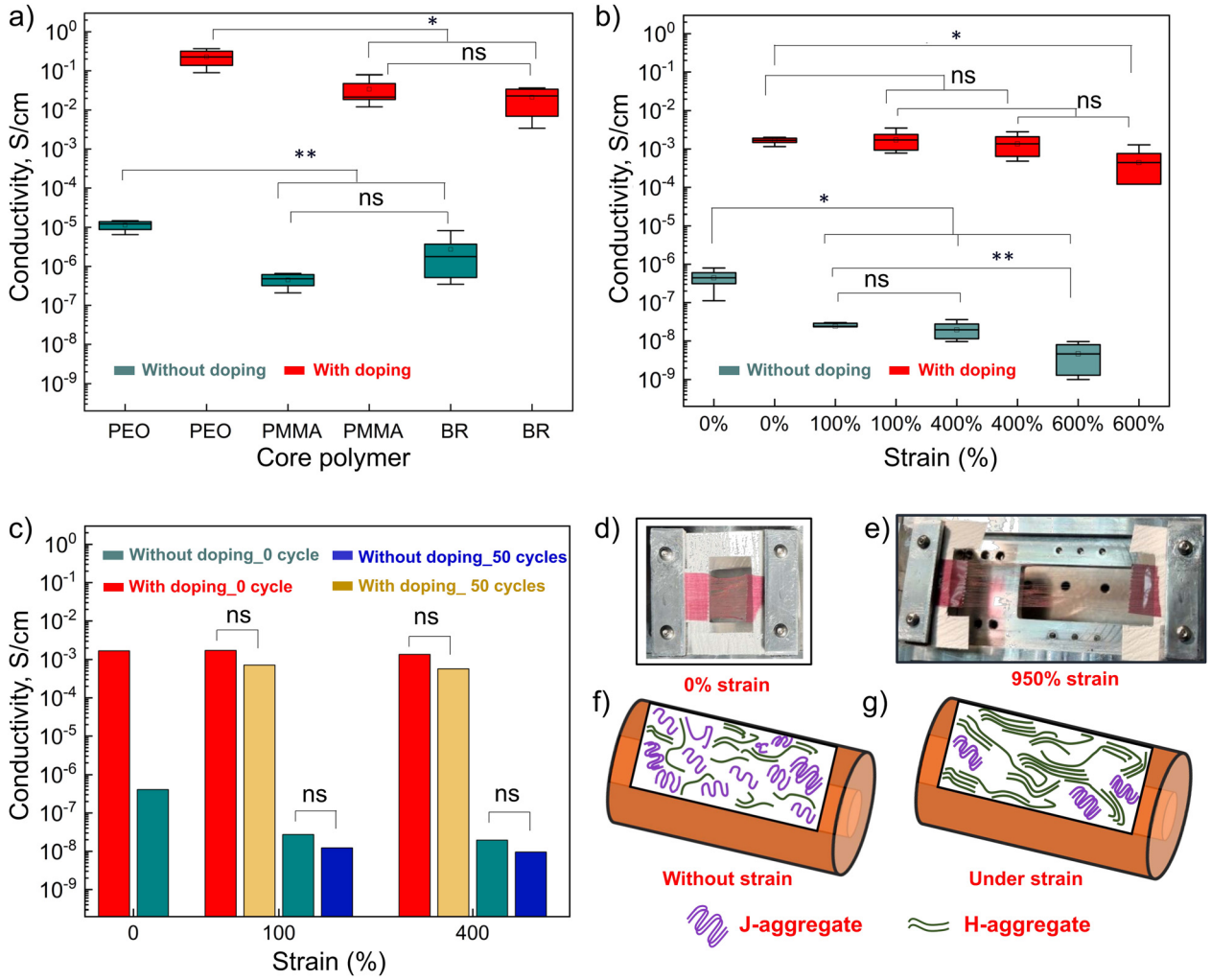

Fig. 5 (a) Electrical conductivity (σ) of doped and undoped fibers with different core polymers at unstretched (0% strain) condition; (b) σ of P3HT_BR fiber mat under different applied strain; (c) σ of P3HT_BR fiber mat before and after stretching for 50 cycles; (d) experimental setup displaying fiber mat collected on a paper cut for mechanical testing, (e) P3HT_BR fiber mat stretched to 950% of the initial length; (f) and (g) Schematic representations of J- and H-aggregates of P3HT in the shell of electrospun fiber: without stretch (f), stretched (g). Two-tailed t-test was used for statistical analysis, where $n \geq 6$; *$p < 0.05$; **$p < 0.01$, and ns indicates not significant.

statistically higher than the P3HT_PMMA and P3HT_BR. This can be attributed to the larger fiber diameters and corresponding larger core diameters for P3HT_PMMA and P3HT_BR affecting the estimation of conductivity. We can also compare the σ of coaxial fibers with our previously reported uniaxial P3HT_PEO fibers, where P3HT was mixed with PEO and was electropsun.[35] We observed that the σ for coaxial fibers was similar to that of uniaxial fibers, spun from the aged P3HT solution (allowing self-assembly in the solution state) but not for the case where fresh P3HT was considered.[35]

P3HT on the shell also enables direct doping of the fibers. The doping with F4TCNQ has led to the increase of σ to 2.3×10^{-1}, 2.2×10^{-2}, and 2.4×10^{-2} S cm^{-1} for the P3HT_PEO, P3HT_PMMA, and P3HT_BR fibers, respectively. Note that the sequential doping using acetonitrile leaves F4TCNQ anions to remain only in amorphous domains, whereas hole in the crystalline domains of P3HT, allowing high conductivity.[41]

3.3.2. Conductivity of stretched fibers. A custom-built setup (Fig. S1b, ESI†) was used to stretch the fiber mats to a prescribed strain value. Here, fiber mats instead of single fiber were used for experimental simplicity. We determined the maximum stretchability of P3HT_PEO and P3HT_BR fiber mats based on the fracture onset strain. The P3HT_BR fibers demonstrated a high fracture onset strain of ~1000% (Fig. S10g and Video S1, ESI†), whereas that for P3HT_PEO was ~350%. P3HT_BR fibers without an applied strain and at 950% strain are presented in Fig. 5d and e. The P3HT-BR fibers could be reversibly stretched and unstretched multiple times. The high stretchability and reversibility of these fibers can be attributed to the stretchable elastomer (BR) core. In contrast, the P3HT_PEO fiber mat showed strong hysteresis/irreversibility, likely due to the yielding of semicrystalline PEO at high strain. The doping process did not significantly affect the stretchability and reversibility.

The σ of P3HT_BR fiber mats was measured at different strain conditions, ranging from unstretched (0%) to 600%, both with and without F4TCNQ doping (Fig. 5b). The σ decreased by an order of magnitude (4.1×10^{-7} to 2.73×10^{-8} S cm^{-1}) when the fiber mat was stretched from 0% to 100% for undoped samples. The σ then mostly remained unchanged up to 400% strain but decreased significantly at strain values beyond that. On the contrary, the conductivity of doped fibers did not change significantly up to 400% strain (1.68×10^{-3} S cm^{-1} at 0% strain to 1.36×10^{-3} S cm^{-1} at 400% strain) but decreased beyond that. This deterioration in charge-transport properties at higher strain could be due to irreversible structural change, such as the dissociation of P3HT crystallites under high strain.[11,29] Note that the estimated σ values of fiber mats were lower than those obtained for single fibers. This can be attributed to the discontinuous nature of fiber mats.

The P3HT_BR fiber mat, both doped and undoped, was subjected to fifty cyclic loadings at 100% and 400% strain (Fig. 5c). The conductivity decreased only slightly after fifty cycles in comparison to that observed after one stretching at both strain percentages, regardless of the doping conditions. This result implies that the P3HT_BR fiber has good mechanical and electrical durability.

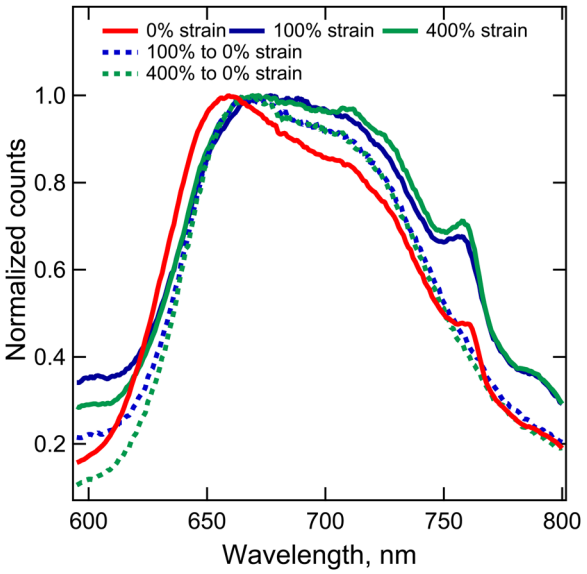

Fig. 6 PL spectra of P3HT_BR fiber mats subjected to different strain values and after released from applied strain.

The PL spectra of the P3HT_BR fiber mat subjected to strain and after being released from the applied strain were obtained to understand the microstructural change due to stretching (Fig. 6). The results for stretching were similar to that presented in Fig. 4b. After releasing the strain, the intensity of the 0-1 transition peak decreased, accompanied by a blue-shifted 0-0 transition from 679 nm to 667 nm. However, the peaks did not return to the positions observed for as-spun fibers. It is likely that the interchain interactions dissociated during the release of strain to 0% because of the low dissociation energy for π–π stacking.[42–44]

Based on the results above, the microstructure change during stretching has been schematically represented in Fig. 5f and g. An applied electric field during electrospinning facilitates the formation of J- and H-aggregates in fiber, with dominant J-aggregates (Fig. 5f). When subjected to uniaxial stretch, the sliding/unfolding of polymer chains and subsequent alignment in the amorphous chains leads to increasing π–π interaction resulting in higher H-aggregate.[11] Note that a decreasing interchain interaction and corresponding blue shift because of stretching was reported by Chen *et al.* for coaxial fibers with P3HT at the core and PEO at the shell.[29]

With mechanical loading, the interchain interaction of amorphous chains increases, leading to short-range ordered aggregates (H-aggregate). Further, the more planar structure of the stretched chains can lead to higher conjugation length.[45,46] Both of these can increase the conductivity.[47] On the other hand, mechanical loading can lead to the yielding and dissociation of P3HT crystallites, as for P3HT thin films, the yield strain has been determined to be ≈100–150%.[48,49] The dissociation of the crystallite structure would decrease the conductivity.[11] The combinations of all these factors dictate the conductivity. The above data indicate that the yielding and dissociation of P3HT crystallites were dominant in degrading the charge-transport properties, particularly at higher strain values, *viz.*, 600%.[11,50] However,

doping can be used to overcome the change in conductivity values at lower applied strain (Fig. 5c).

Note that the BR-based electrospun fibers obtained here displayed higher fracture strain values than the reported P3HT coaxial fiber systems.[17,29] However, stress–strain data from single fibers experiments will be needed to better understand these systems' mechanical responses. Fiber processed using our proposed method does not require any post-treatment for characterization and the subsequent doping process. In contrast, most of the literature reports on the core–shell ES fibers indicated the removal of shell polymers, as CPs were in the core for those cases.[29,32,34] This removal process could significantly deteriorate the performance of the CPs in the core. Our framework allows the use of different core polymers. Similarly, various donor–acceptor semiconducting polymers can be processed at the shell-side to obtain stretchable fibers. The electrical conductivity data obtained for our fibers cannot be directly compared to other ES fiber systems, as many of those were investigated in OFET devices. Future research will include the investigation of our system in OFET devices. We would like to note that the electrical conductivity values of P3HT thin films doped with F4TCNQ are available in the literature, and our conductivity values are of the same order as those for the similar F4TCNQ concentration considered here.[51–53]

4. Conclusions

In summary, we have demonstrated the fabrication of highly stretchable electrospun P3HT fibers utilizing coaxial electrospinning techniques. The polarized optical microscopy analysis shows the ordered structure present in the fibers. PL spectroscopic analysis of the fiber mat captured the redshift of as high as 20 nm for 0-0 aggregation peak in the stretched fibers. Also, it has been seen that the intensity of the 0-1 aggregation peak slightly increases with applied strain. This occurs as a result of the polymer chains sliding or unfolding in the amorphous region to form a short-range (H-aggregate) alignment. Moreover, the coaxial P3HT_BR fiber demonstrated excellent stretchability by displaying an excellent onset fracture strain of approximately 1000% strain. The electrical conductivity of the undoped fibers decreased by an order of magnitude subjected to 100% strain but did not decrease further under cyclic loading, showing outstanding mechanical and electrical durability. Our results provide new understandings linking the processing of conjugated polymers in fibers, the polymer structure in these fibers, and the change of structure and electrical properties with mechanical loading. Such information will be useful for these polymers' potential applications in flexible electronic devices and others.

Author contributions

SK and HA designed the experiments, and HA conducted the experiments. MB conducted initial experiments. MG assisted in analyzing conductivity data. SK oversaw the research. HA and SK conducted the data analysis and interpretation. The manuscript was written by HA and SK.

Conflicts of interest

There are no conflicts to declare.

Acknowledgements

This work is based on work supported by the National Science Foundation under Grant No. 1757220 (OIA 1757220).

References

1 W. Weng, P. Chen, S. He, X. Sun and H. Peng, *Angew. Chem., Int. Ed.*, 2016, 6140–6169.
2 J. A. Rogers, T. Someya and Y. Huang, *Science*, 2010, **327**(5973), 1603–1607.
3 Z. Bao and X. Chen, *Adv. Mater.*, 2016, 4177–4179.
4 Y. Ding, W. Xu, W. Wang, H. Fong and Z. Zhu, *ACS Appl. Mater. Interfaces*, 2017, **9**(35), 30014–30023.
5 K. Gu and Y. L. Loo, *J. Polym. Sci., Part B: Polym. Phys.*, 2019, **57**, 1559–1571.
6 D. T. Scholes, P. Y. Yee, J. R. Lindemuth, H. Kang, J. Onorato, R. Ghosh, C. K. Luscombe, F. C. Spano, S. H. Tolbert and B. J. Schwartz, *Adv. Funct. Mater.*, 2017, **27**, 1–13.
7 N. Kleinhenz, C. Rosu, S. Chatterjee, M. Chang, K. Nayani, Z. Xue, E. Kim, J. Middlebrooks, P. S. Russo, J. O. Park, M. Srinivasarao and E. Reichmanis, *Chem. Mater.*, 2015, **27**, 2687–2694.
8 L. A. Perez, P. Zalar, L. Ying, K. Schmidt, M. F. Toney, T. Q. Nguyen, G. C. Bazan and E. J. Kramer, *Macromolecules*, 2014, **47**, 1403–1410.
9 J. Mun, Y. Ochiai, W. Wang, Y. Zheng, Y. Zheng, H. Wu, N. Matsuhisa, T. Higashihara, J. B. Tok, Y. Yun and Z. Bao, *Nat. Commun.*, 2021, 1–10.
10 M. Lakdusinghe, M. Mooney, H. Ahmad, I. Chu, S. Rondeau-gagn and S. Kundu, *Langmuir*, 2023, **39**(35), 12283–12291.
11 Y. Zheng, S. Zhang, B. Tok and Z. Bao, *J. Am. Chem. Soc.*, 2022, **144**(11), 4699–4715.
12 S. Zhang, Y. H. Cheng, L. Galuska, A. Roy, M. Lorenz, B. Chen, S. Luo, Y. T. Li, C. C. Hung, Z. Qian, P. B. J. St. Onge, G. T. Mason, L. Cowen, D. Zhou, S. I. Nazarenko, R. F. Storey, B. C. Schroeder, S. Rondeau-Gagné, Y. C. Chiu and X. Gu, *Adv. Funct. Mater.*, 2020, **30**, 1–10.
13 J. Y. Chen, H. C. Hsieh, Y. C. Chiu, W. Y. Lee, C. C. Hung, C. C. Chueh and W. C. Chen, *J. Mater. Chem. C*, 2020, **8**, 873–882.
14 R. Peng, B. Pang, D. Hu, M. Chen, G. Zhang, X. Wang, H. Lu, K. Cho and L. Qiu, *J. Mater. Chem. C*, 2015, **3**, 3599–3606.
15 S. Zhang, Y. H. Cheng, L. Galuska, A. Roy, M. Lorenz, B. Chen, S. Luo, Y. T. Li, C. C. Hung, Z. Qian, P. B. J. St. Onge, G. T. Mason, L. Cowen, D. Zhou, S. I. Nazarenko,

R. F. Storey, B. C. Schroeder, S. Rondeau-Gagné, Y. C. Chiu and X. Gu, *Adv. Funct. Mater.*, 2020, 2000663.
16 D. Choi, H. Kim, N. Persson, P. Chu, M. Chang, J. Kang, S. Graham and E. Reichmanis, *Chem. Mater.*, 2016, **28**(4), 1196–1204.
17 M. Y. Lee, Y. Oh, J. Hong, S. J. Lee, D. G. Seong, M. K. Um and J. H. Oh, *Adv. Electron. Mater.*, 2021, **7**, 1–9.
18 M. Ashizawa, Y. Zheng, H. Tran and Z. Bao, *Prog. Polym. Sci.*, 2020, **100**, 101181.
19 D. J. Lipomi and Z. Bao, *MRS Bull.*, 2017, **42**, 93–97.
20 M. Mohanan, H. Ahmad, P. Ajayan, P. K. Pandey, B. M. Calvert, X. Zhang, F. Chen, S. J. Kim, S. Kundu and N. Gavvalapalli, *Chem. Sci.*, 2023, **14**, 5510–5518.
21 M. Shin, J. Y. Oh, K. Byun, Y. Lee, B. Kim, H. Baik, J. Park and U. Jeong, *Adv. Mater.*, 2015, **27**, 1255–1261.
22 E. Song, B. Kang, H. H. Choi, D. H. Sin, H. Lee, W. H. Lee and K. Cho, *Adv. Electron. Mater.*, 2016, **2**, 1500250.
23 H. Wu, S. J. Benight, A. Chortos, W. Lee, J. Mei, J. W. F. To, C. Lu, M. He, B. Tok, W. Chen and Z. Bao, *Chem. Mater.*, 2014, **26**, 4544–4551.
24 R. Peng, B. Pang, D. Hu, M. Chen and G. Zhang, *J. Mater. Chem. C*, 2015, **3**, 3599–3606.
25 J. Y. Oh, S. Rondeau-gagné, Y. Chiu, A. Chortos, F. Lissel, G. N. Wang, B. C. Schroeder, T. Kurosawa, J. Lopez, T. Katsumata, J. Xu, C. Zhu, X. Gu, W. Bae, Y. Kim, L. Jin, J. W. Chung, J. B. Tok and Z. Bao, *Nature*, 2016, **539**, 411–415.
26 M. Shin, J. Y. Oh, K. Byun, Y. Lee, B. Kim, H. Baik, J. Park and U. Jeong, *Adv. Mater.*, 2015, **27**(7), 1255–1261.
27 H. Cheng, S. Zhang, L. Michalek, X. Ji, S. Luo, C. B. Cooper, H. Gong, S. Nikzad, J. A. Chiong, Y. Wu, Y. Zheng, Q. Liu, D. Zhong, Y. Lei, Y. Tomo, K. Wei, D. Zhou, J. B. Tok and Z. Bao, *ACS Mater. Lett.*, 2022, **4**(11), 2328–2336.
28 J. Xu, S. Wang, G.-J. Nathan Wang, C. Zhu, S. Luo, L. Jin, X. Gu, S. Chen, V. R. Feig, J. W. F. To, S. Rondeau-Gagné, J. Park, B. C. Schroeder, C. Lu, J. Young Oh, Y. Wang, Y.-H. Kim, H. Yan, R. Sinclair, D. Zhou, G. Xue, B. Murmann, C. Linder, W. Cai, J. B.-H. Tok, J. Won Chung and Z. Bao, *Science*, 2017, **355**, 59–64.
29 J. Y. Chen, H. C. Hsieh, Y. C. Chiu, W. Y. Lee, C. C. Hung, C. C. Chueh and W. C. Chen, *J. Mater. Chem. C*, 2020, **8**, 873–882.
30 F. Pierini, M. Lanzi, P. Nakielski, S. Pawłowska, K. Zembrzycki and T. A. Kowalewski, *Polym. Adv. Technol.*, 2016, **27**, 1465–1475.
31 J. Y. Chen, H. C. Wu, Y. C. Chiu, C. J. Lin, S. H. Tung and W. C. Chen, *Adv. Electron. Mater.*, 2015, **1**, 3–6.
32 J. Y. Chen, C. C. Kuo, C. S. Lai, W. C. Chen and H. L. Chen, *Macromolecules*, 2011, **44**, 2883–2892.
33 C. Zhu, J. Wu, J. Yan and X. Liu, *Adv. Fiber Mater.*, 2023, **5**, 12–35.
34 J. Y. Chen, H. C. Wu, Y. C. Chiu, C. J. Lin, S. H. Tung and W. C. Chen, *Adv. Electron. Mater.*, 2015, **1**, 1–8.
35 H. Ahmad, S. Zhang, C.-T. Liu, G. Ma, J. D. Azoulay, X. Gu, M. K. Gangishetty and S. Kundu, *ACS Appl. Polym. Mater.*, 2022, **4**, 8812–8824.
36 P. Filip and P. Peer, *Processes*, 2019, **7**(12), 948.
37 C. Y. Chen, S. H. Chan, J. Y. Li, K. H. Wu, H. L. Chen, J. H. Chen, W. Y. Huang and S. A. Chen, *Macromolecules*, 2010, **43**, 7305–7311.
38 F. C. Spano, *Acc. Chem. Res.*, 2010, **43**, 429–439.
39 D. Kajiya and K. I. Saitow, *ACS Appl. Energy Mater.*, 2018, **1**, 6881–6889.
40 F. C. Spano and C. Silva, *Annu. Rev. Phys. Chem.*, 2014, **65**, 477–500.
41 I. E. Jacobs, E. W. Aasen, J. L. Oliveira, T. N. Fonseca, J. D. Roehling, J. Li, G. Zhang, M. P. Augustine, M. Mascal and A. J. Moulé, *J. Mater. Chem. C*, 2016, **4**, 3454–3466.
42 N. Rai and J. I. Siepmann, *J. Phys. Chem. B*, 2007, **111**, 10790–10799.
43 S. Tsuzuki, K. Honda and R. Azumi, *J. Am. Chem. Soc.*, 2002, **124**(41), 12200–12209.
44 F. Rodríguez-Ropero, J. Casanovas and C. Alemán, *J. Comput. Chem.*, 2008, **29**, 69–78.
45 C. M. Wolf, L. Guio, S. C. Scheiwiller, R. P. O'Hara, C. K. Luscombe and L. D. Pozzo, *Macromolecules*, 2021, **54**, 2960–2978.
46 A. R. Aiyar, J. Il Hong and E. Reichmanis, *Chem. Mater.*, 2012, **24**, 2845–2853.
47 S. Savagatrup, X. Zhao, E. Chan, J. Mei and D. J. Lipomi, *Macromol. Rapid Commun.*, 2016, 1–6.
48 B. O'Connor, E. P. Chan, C. Chan, B. R. Conrad, L. J. Richter, R. J. Kline, M. Heeney, I. McCulloch, C. L. Soles and D. M. DeLongchamp, *ACS Nano*, 2010, **4**, 7538–7544.
49 D. Rodriquez, J. H. Kim, S. E. Root, Z. Fei, P. Boufflet, M. Heeney, T. S. Kim and D. J. Lipomi, *ACS Appl. Mater. Interfaces*, 2017, **9**(10), 8855–8862.
50 T. Zhang, L. Zhang, S. Wang, J. Li, J. Zuo, R. Chen, X. Yu, J. Peng, Q. Zhang and Y. Han, *Polymer*, 2023, **278**, 125986.
51 I. Salzmann, G. Heimel, M. Oehzelt, S. Winkler and N. Koch, *Acc. Chem. Res.*, 2016, **49**(3), 370–378.
52 E. Lim, K. A. Peterson, G. M. Su and M. L. Chabinyc, *Chem. Mater.*, 2018, **30**(3), 998–1010.
53 I. E. Jacobs, E. W. Aasen, J. L. Oliveira, T. N. Fonseca, J. D. Roehling, J. Li, G. Zhang, M. P. Augustine, M. Mascal and A. J. Moulé, *J. Mater. Chem. C*, 2016, **4**(16), 3454–3466.

